Combined effects of contact friction and particle shape on strength properties and microstructure of sheared granular media

Theechalit Binaree,[1,*] Emilien Azéma,[2,†] Nicolas Estrada,[3,‡] Mathieu Renouf,[2,§] and Itthichai Preechawuttipong[1,‖]

[1]*Department of Mechanical Engineering, Faculty of Engineering, Chiang Mai University, 239 Huay Kaew Road, Chiang Mai 50200, Thailand*

[2]*LMGC, Université de Montpellier, CNRS, Montpellier, France*

[3]*Departamento de Ingeniería Civil y Ambiental, Universidad de Los Andes, Bogotá, Colombia*

(Received 19 March 2020; accepted 16 July 2020; published 3 August 2020)

We present a systematic numerical investigation concerning the combined effects of sliding friction and particle shape (i.e., angularity) parameters on the shear strength and microstructure of granular packings. Sliding friction at contacts varied from 0 (frictionless particles) to 0.7, and the particles were irregular polygons with an increasing number of sides, ranging from triangles to disks. We find that the effect of local friction on shear strength follows the same trend for all shapes. Strength first increases with local friction and then saturates at a shape-dependent value. In contrast, the effect of angularity varies, depending on the level of sliding friction. For low friction values (i.e., under 0.3), the strength first increases with angularity and then declines for the most angular shapes. For high friction values, strength systematically increases with angularity. At the microscale, we focus on the connectivity and texture of the contact and force networks. In general terms, increasing local friction causes these networks to be less connected and more anisotropic. In contrast, increasing particle angularity may change the network topology in different directions, directly affecting the macroscopic shear strength. These analyses and data constitute a first step toward understanding the joint effect of local variables such as friction and grain shape on the macroscopic rheology of granular systems.

DOI: 10.1103/PhysRevE.102.022901

I. INTRODUCTION

In general terms, the shear strength of an assembly of dry rigid particles can be characterized through a macroscopic friction coefficient $\mu = \tau/\sigma$, where τ is the maximal shear stress that can be applied to a plane with normal stress σ [1]. During shear deformation, a basic observation is that μ first increases; depending on whether the system is dense or loose, it may pass through a peak and then reach a steady state after a sufficiently large deformation. This steady state is called the "critical state" in soil mechanics [1] and is usually characterized by a friction coefficient μ^* and a solid fraction ρ^*, which are interesting because they are independent of the initial configuration. In other words, in this state the memory of the initial configuration has been totally erased by means of the particles' rearrangements.

Macroscopic friction results from both the sliding friction at the contacts, which is characterized by a local friction coefficient μ_s, and the typical disorder of granular arrangements that is induced by particle sizes and shapes. It is known that μ^* first increases with μ_s and then saturates at a constant value, irrespective of μ_s. This has been shown for packings made of disks [2–8], and more recently for packings made of cubelike particles [9] and irregular-shaped structures [10]. Discrete element simulations have also revealed that less than half of the contacts fully mobilize their frictional strength. This suggests that sliding is not the dominant mechanism of relative motion between particles, but that rolling also plays an important role in this process [6,11].

Several numerical studies have confirmed the major role played by particle rotation in the strength and deformation of granular media [12–16]. Specifically, if the relative rotation between particles is constrained through rolling resistance, then the local environment is strongly affected leading to higher values of μ^* [6,17–20]. This explains why it is difficult to obtain realistic values of macroscopic friction using model granular media composed of circular or spherical particles interacting through sliding friction.

In dry granular media, the restriction of particle rotations is a consequence of the nonspherical particle shape [21]. A general observation is that μ^* increases as the particle shape deviates even slightly from a circle or a sphere, but then tends to saturate with shape deviation [22–29]. Another interesting result concerns the ideal case of frictionless grains. For these, a nonzero (although weak) value of μ^* is observed [30–32].

Thus, existing results suggest that local friction and particle shape strongly affect the macroscopic properties of an assembly of grains. The pending issue is the joint effect of the two parameters on the rheology of sheared granular media. We address this question in the paper and propose a systematic analysis of the interplay between mechanical effects (induced

*theechalit_b@cmu.ac.th
†emilien.azema@umontpellier.fr
‡n.estrada22@uniandes.edu.co
§mathieu.renouf@umontpellier.fr
‖itthichai.p@cmu.ac.th

by friction) and geometrical effects (induced by shape). The local friction coefficient varied from 0 (frictionless systems) to 0.7, and the shape of the particles varied from disks to triangles. We only considered packings composed of polygonal particles, since their shape can be easily controlled through the number of their sides.

Below, in Sec. II we introduce the numerical approach, system characteristics, and loading parameters. In Sec. III we present a parametric study of the strength and density of the systems, as functions of local friction and particle angularity. Section IV is devoted to the analysis of the contact network: connectivity and texture. The results are summarized and discussed in Sec. V, together with some perspectives.

II. NUMERICAL PROCEDURES

A. Simulation method

The simulations were carried out by means of the contact dynamics (CD) method, which is suitable for simulating large assemblies of rigid massive particles [23,33–35]. In this method, the equations of motion (i.e., Newton's laws) are integrated over a small time step and combined with the kinematic constraints resulting from contact interactions. These interactions are characterized by three parameters: the coefficient of friction μ_s and the coefficients restitution in the normal and tangential directions, which control the rate of energy dissipation. Contact interactions are thus rewritten as complementarity relations between velocity changes and impulses; the normal interaction is described by the Signorini condition and the tangential interaction is described through Coulomb's friction law. In other words, contact laws are not regularized, as is the case in smooth approaches such as the molecular dynamics (MD) method and the like. Moreover, since small contact deformations do not need to be resolved to calculate the forces, the time step can be larger than in MD. In CD, an iterative and parallelized algorithm [36] based on a nonlinear Gauss-Seidel scheme is used to determine the contact forces and particle velocities simultaneously at all potential contacts. It must be noted that in all the simulations presented in this paper the restitution coefficients are set to zero. In fact, it has been shown that the quasistatic behavior of sheared granular systems is independent of the coefficient of restitution unless this parameter is set to very large values (i.e., above 0.8) [37]. For an explanation of the specific implementation of the method, see Refs. [34,35].

When treating contacts between polygonal particles, three situations may arise: side-to-side (ss) contacts, side-to-vertex (sv) contacts, and vertex-to-vertex (vv) contacts; see Fig. 1. For sv contacts, a single contact point is used, and the normal vector lies perpendicular to the side. ss contacts are represented by two points located along the sides that touch each other (i.e., the points located at the extremities of the contact segment), and the normal vector is perpendicular to these common sides. Numerically, this means that two forces are calculated. However, physically only their resultant and application points are of interest. vv contacts are rare, but when such a situation arises they are treated as ss or sv contacts, depending on the path followed by the two particles. Note that a complete description of the CD method is presented in the annex in [23], including the special treatment for contacts between polygonal particles.

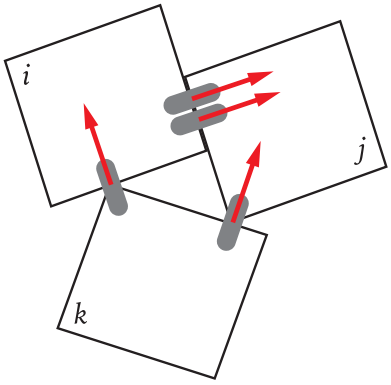

FIG. 1. Examples of the most common types of contacts between polygonal particles: side-to-vertex (sv) contacts between pairs of particles $\{k, i\}$ and $\{k, j\}$, and side-to-side (ss) contact between the pair of particles $\{i, j\}$. The red arrows represent the unit normal vector.

We used the LMGC90 open-source platform, developed in the University of Montpellier, France. This is extensively employed in research on the simulation of granular materials, in two and three dimensions, with particles of arbitrary shape, size, and with different types of mechanical behavior.[1]

B. Packing construction and biaxial tests

Our numerical samples were composed of $N_p = 10000$ particles placed in a rectangular box bounded by frictionless walls, with density ρ and with diameters (i.e., circumscribed circles) d varying between $d_{\min} = 0.8 d_{\max}$ and $d_{\max}$, with a uniform distribution of particle volume fractions (i.e., each size class occupies the same volume in the sample), where $d_{\max}$ is the maximum diameter. A set of 11 different packings was prepared, each composed of particles having the same number of sides: one packing of disks and 10 packings with $n_s \in [50, 30, 20, 10, 8, 7, 6, 5, 4, 3]$. In other words, the angularity of the particles, defined as $\alpha = 2\pi/n_s$, varied from 0 (disks) to $2\pi/3$ (triangles). To avoid local ordering, slightly irregular polygons were used. The level of irregularity was controlled by randomly perturbing the position θ_i of each vertex i according to the simple formula: $\theta_i = \theta_0 + 2\pi i/n_s \pm \delta\pi/n_s$ [38], with $\delta = 0.3$. In the following, particle-wall friction and gravity were set to zero in all our simulations.

First, a dense packing of disks was constructed by means of a layer-by-layer deposition model, such as those described in Ref. [39]. Basically, the disks were deposited sequentially on a substrate. Each new disk was placed at the lowest possible position at the free surface as a function of its diameter. This procedure produced a dense packing in which each disk was supported by two underlying disks. For polygonal particles, the same disk packing was used, with each disk serving as the circumscribing circle of a polygonal particle. The latter

[1]LMGC90 (2018), https://git-xen.lmgc.univ-montp2.fr/lmgc90/lmgc90_user/wikis/home.

was inscribed with the given value of α and at a random orientation. Then, each packing was compressed isotropically by applying a stress σ_0 on all walls. During this phase, sliding friction μ_s was set to zero, both between particles and between particles and walls. This procedure allowed to obtain dense systems, similar to the so-called random close packing state. Figure 2 shows several particle-scale views at the end of the isotropic compression phase, for different values of n_s.

Second, the isotropically prepared samples were biaxially sheared by imposing a vertical velocity v_y on the upper wall while maintaining a confining stress σ_0 on the lateral walls. The velocity v_y was such that tests could be considered to be in the quasi-static limit. This was quantified through the inertial number I, defined as [40]

$$I = \frac{v_y}{H} d \sqrt{\frac{\rho}{\sigma_0}}, \tag{1}$$

where H is the sample height, ρ is the particle density, and d is the mean diameter. In all our simulations, I was equal to 5×10^{-4}. Starting from the same dense samples, several biaxial tests were conducted, one for each value of the interparticle friction $\mu_s \in [0, 0.01, 0.05, 0.1, 0.2, 0.3, 0.4, 0.5, 0.6, 0.7]$, while keeping the coefficient of friction with the walls and the gravity equal to 0. Hence, a total of 121 simulations were performed: 11 isotropic compressions with $\mu_s = 0$ and $\alpha \in [0, 2\pi/3]$ and 110 biaxial shears for $\mu_s \in [0, 0.7]$ and $\alpha \in [0, 2\pi/3]$.

III. STRENGTH AND PACKING FRACTIONS

A. Definitions

As was explained in the Introduction, the shear strength of an assembly of grains can be described using the ratio of the shear to normal stress $\mu = \tau/\sigma$. However, in a biaxial geometry it is more convenient to express the macroscopic friction in terms of the invariants of the stress tensor. Let σ_i, with $i \in \{1, 2\}$ in 2D, be the principal stresses. The average stress is given by $p = (\sigma_1 + \sigma_2)/2$, and the deviatoric stress can be written as $q = (\sigma_1 - \sigma_2)/2$. Then, using the Mohr representation and the Coulomb failure criterion, it can be shown that $\mu \simeq q/p$ [41].

To calculate the stress tensor $\boldsymbol{\sigma}$, we used the formula based on the averages of the "tensorial moment" $\boldsymbol{M}^{\xi}$ of the particles ξ in a volume (area in 2D) V [42] that is now considered classical:

$$\boldsymbol{\sigma} = \frac{1}{V} \sum_{\xi \in V} \boldsymbol{M}^{\xi}, \tag{2}$$

with

$$\boldsymbol{M}^{\xi}_{ij} = \sum_{c \in \xi} f^c_i r^c_j, \tag{3}$$

where f^c_i is the i component of the force exerted on a particle ξ in contact c, r^c_j is the j component of the position vector of the same contact, and the sum runs over all the contact neighbors of the particle ξ.

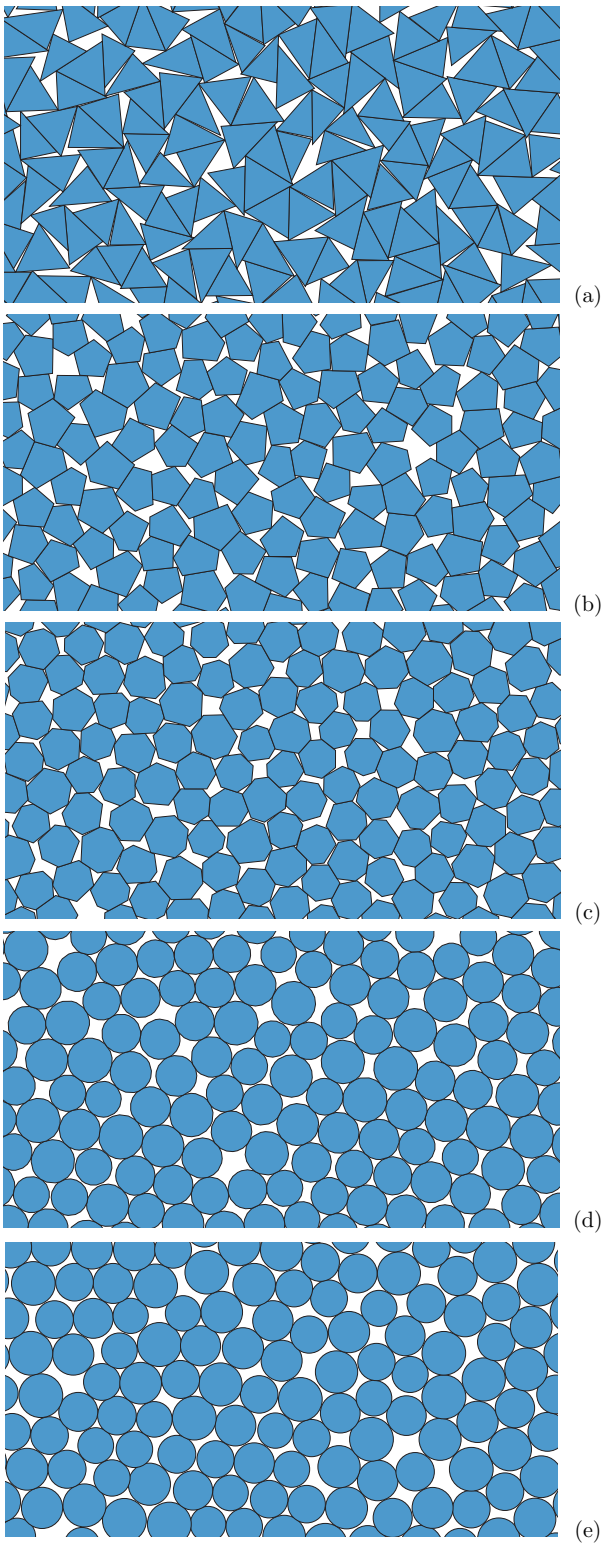

FIG. 2. Particle-scale views of the some of the packings generated in the isotropic compression phase: (a) $n_s = 3$, (b) $n_s = 5$, (c) $n_s = 7$, (d) $n_s = 20$, and (e) disks.

The packing fraction ρ is defined as the ratio V_p/V, where V_p is the volume occupied by the particles and V is the total volume. The vertical strain ε_1 is defined as $\Delta h/h_0$, where $\Delta h = h_0 - h$ is the downward displacement of the upper wall, h_0 is the initial height and h is the height.

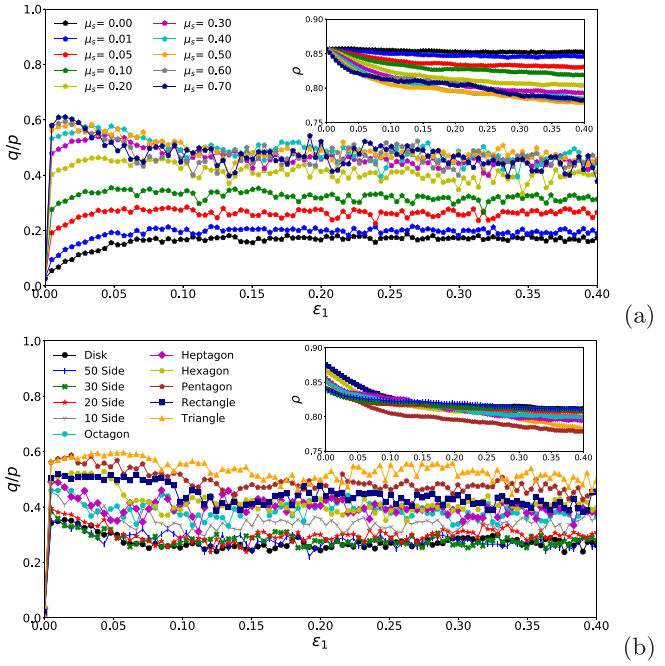

FIG. 3. Stress ratio q/p and solid fraction ρ (insets) as functions of the vertical strain ε_1. (a) Packings of pentagons for all values of the local friction μ_s. (b) Packings with $\mu_s = 0.5$ for all shapes.

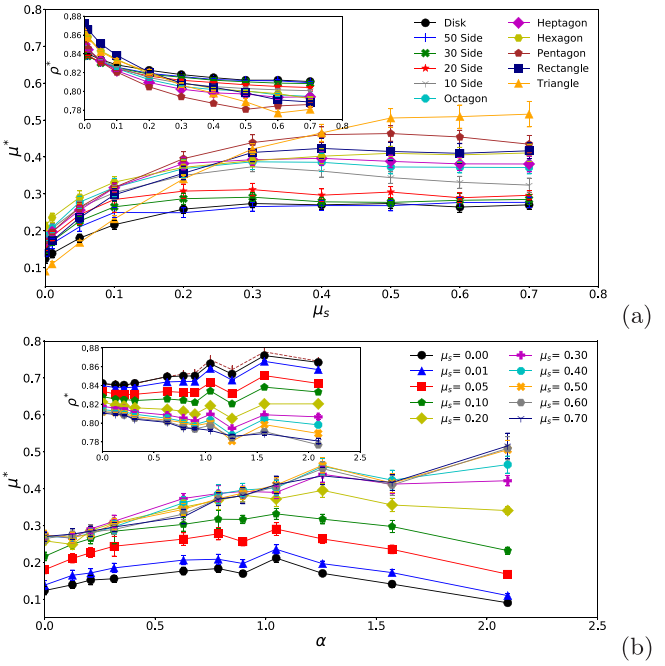

FIG. 4. Macroscopic friction coefficient μ^* and packing fraction ρ^* (insets) in the steady state, as functions of both the local friction μ_s (a) and the particle angularity α (b). The dashed line in the inset of (b) represents the initial solid fraction ρ_0. Error bars represent the standard deviation in the steady state.

B. Stress-strain behavior

Figure 3 shows the evolution of the stress ratio q/p and the packing fraction ρ (insets) as functions of the vertical strain ε_1. It can be seen that for the lowest values of the local friction μ_s the stress ratio q/p first increases and then stabilizes at a constant value within fluctuations. In contrast, for the largest values of μ_s (i.e., for $\mu_s > 0.1$) q/p passes through a maximum before decreasing and stabilizing. Hence, an important remark is that the existence of the strength peak cannot be attributed exclusively to high values of the packing fraction (all samples are initially dense) but also involves friction between particles. We also observe that within a good approximation a constant shear strength is reached for $\varepsilon_1 \gtrsim 0.3$. In the following, all reported quantities correspond to the mean values in the steady state (i.e., for $\varepsilon_1 > 0.3$), and they are thus independent of the initial configuration of the samples. As mentioned in Sec. II B, all samples are initially dense. For this reason, ρ decreases from its initial value ρ_0 and stabilizes at a practically constant value for larger ε_1. It can be noted that dilation diminishes with $\mu_s \to 0$, and, remarkably, no dilation is observed in the limit of frictionless particles. This observation is consistent with previous results obtained for packings of frictionless disks, pentagons, and spheres [30,31,43].

Figure 4 shows the macroscopic friction coefficient μ^* and the packing fraction ρ^* (defined from the mean values of q/p and ρ, respectively, in the steady state) as functions of both the local friction μ_s and the particle angularity α. For all shapes, μ^* first increases with μ_s and then saturates at a shape-dependent value. These results extend to the family of polygonal particles a similar behavior to that observed for disks, spheres, and cubelike particles [4,6,8,9,44]. It can be noted that a similar trend is followed for all shapes. In contrast, the evolution of μ^* with α depends heavily on μ_s. For weakly frictional systems (i.e., for μ_s below 0.3), μ^* first increases with α but surprisingly it declines as particles become more angular (i.e., for n_s below 6). This means that a weakly frictional packing composed of triangles or squares can have a macroscopic friction that is smaller than that of a packing of disks! For more frictional systems, μ^* is an increasing function of α. This behavior is rather unexpected, and suggests a complex interplay at the microscopic scale, as will be discussed in Sec. IV.

The insets in Fig. 4 show that the evolution of ρ^* with μ_s and α is almost the inverse of that of μ^*. Typically, ρ^* declines with μ_s for all shapes. In contrast, ρ^* increases with α in weakly frictional systems and declines with α for the largest values of μ_s. The initial solid fraction ρ_0 is shown using a dashed line. Remarkably, $\rho^* \simeq \rho_0$ for frictionless particles of all shapes. This confirms that "Frictionless granular packs have macroscopic friction, but no dilatancy" [30] and extends this finding to the family of noncircular particles.

In the following sections, we analyze the micromechanical properties of our packings of polygonal particles with the aim of identifying the origins of the nonlinear variation of the shear strength with local friction and particle angularity.

IV. MICROMECHANICAL ANALYSIS

A. Connectivity

The principal effect of friction is to enhance arching effects inside the material. In contrast, the principal effect of polygonal shapes is to allow for side-to-side contacts, which are

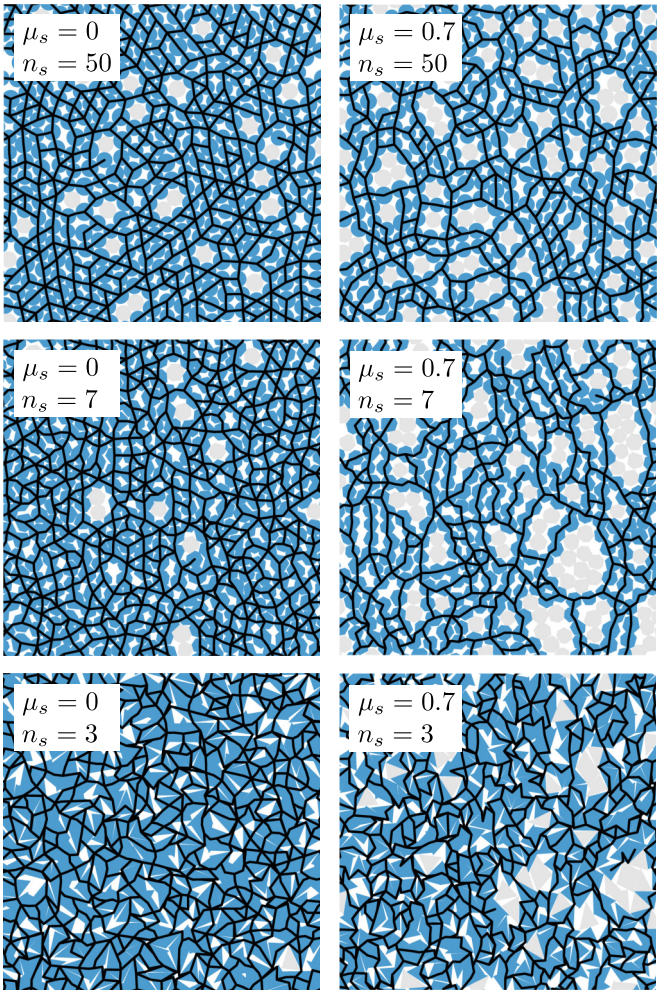

FIG. 5. Particle-scale views of the contact network in six packings, for different values of local friction μ_s and particle angularity α. Contacts are shown as black lines joining the contact points to the center of the particles, and floating particles (i.e., particles with 0 or 1 contact) are shown in light gray.

particularly stable. Thus, both local friction and particle angularity are expected to have a strong effect on the structure of the contact network. As an example, Fig. 5 shows particle-scale views of the contact network of six packings, for different values of local friction μ_s and particle angularity α. Contacts are represented as lines joining the contact points to the center of the particles. Floating grains (i.e., grains with zero or one contact) are shown in light grey. First, it can be seen that the contact network density (i.e., the number of contacts per particle) decreases as μ_s increases. Hence, frictional systems exhibit a larger proportion of floating grains, which tend to group together. Second, it can be seen that increasing μ_s increases the network anisotropy, allowing for the formation of chains of contacts that are more or less oriented along the principal stress direction. Then, it can be observed that for systems with the most angular particles the contact network is more tortuous.

The system's connectivity can be quantified by means of two descriptors: the coordination number Z and the proportion of floating particles P_f. We define $Z = 2N_c/[N_p(1 - P_f)]$,

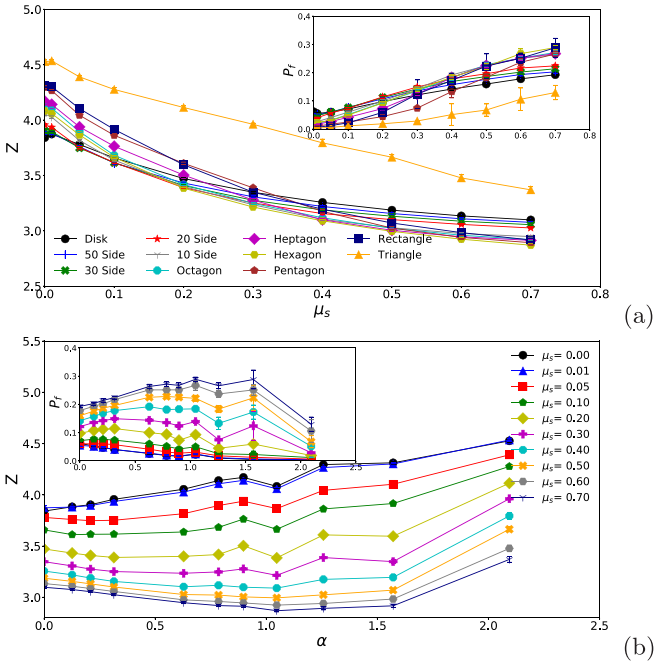

FIG. 6. Coordination number Z and proportion of floating particles P_f (insets) in the steady state, as functions of both the local friction μ_s (a) and the particle angularity α (b). Error bars represent the standard deviation in the steady state.

where N_c is the number of contacts (side-to-side (*ss*) contacts are counted as one contact) and N_p is the number of particles. Then, $P_f = N_p^f/N_p$, where N_p^f is the number of floating particles. Figure 6 shows Z and P_f (insets) in the steady state as functions of both μ_s and α. For all shapes, Z decreases with μ_s and tends to saturate for the largest values of local friction. Values are remarkably close between different shapes, except for triangles. In contrast, the evolution of Z with α depends strongly on μ_s. For weakly frictional systems (i.e., for μ_s below 0.2), Z is an increasing function of α. For more frictional systems, Z first decreases with α but then increases as particles become more angular (i.e., for n_s below 6). The increase of Z with α is explained by the fact that the most angular particles, those with sharper corners, can form contacts that cannot be reached by the less angular particles. However, these results show that this property is hindered by the effect of friction.

The insets in Fig. 6 show that the evolution of P_f with μ_s and α is almost the inverse of that of Z, indicating that arching effects can be reduced or enhanced by angularity, whether the friction is low or high, respectively. It is also interesting to note that Z and μ^* follow opposite trends. This means that the most connected systems are not necessarily those with higher shear strength.

It is interesting to note that for disks (i.e., for $\alpha = 0$) Z varies with μ_s in the range $\mu_s \in [3, 4]$. This is to be expected. In fact, in the frictionless limit the system is isostatic, and $Z \simeq Z_{\text{iso}} = 2D = 4$ for assemblies of disks, with D being the space dimension (2 in our simulations). On the other end, if contact sliding is prohibited, which is partially true in very frictional systems, then $Z \simeq D + 1$ [45,46]. For polygons,

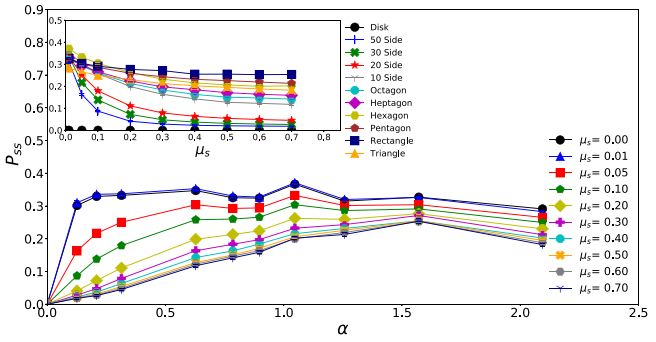

FIG. 7. Proportion of *ss* contacts P_{ss} as a function of both the particle angularity α and the local friction μ_s (inset). Error bars represent the standard deviation in the steady state.

one must consider the rotational degree of freedom, and the connectivity number (defined as the number of constraints per particle, by counting the side-side contacts twice [47]) in the isostatic limit is given by $Z_{c,\mathrm{iso}} = D(D+1) = 6$, which is well verified in our simulations.

Finally, Fig. 7 shows the proportion of *ss* contacts P_{ss} in the steady state as a function of α, for all values of μ_s. Necessarily, $P_{ss} = 0$ for disks (i.e., for $\alpha = 0$). Then, it can be seen that P_{ss} increases with α, since more angular shapes have longer sides which tend to form very stable contacts. We note also that the decrease in P_{ss} to zero as $\alpha \to 0$ is steeper as $\mu_s \to 0$. Such observation is compatible with previous works on assemblies of frictionless spherocylinders, for which a discontinuous variation in P_{ss} is observed as the particles' shape tends to a sphere [48]. We see here that this discontinuity might vanish when one adds interparticle friction. Finally, it can be seen that for all shapes P_{ss} tends to decrease as μ_s increases. This is certainly correlated with the decrease in packing fraction shown in Fig. 4, showing that contact friction allows for more stable structures that depend less on the formation of *ss* contacts.

B. Texture and anisotropy

Figure 8 shows particle-scale views of the normal force network of six packings, for different values of the local friction μ_s and particle angularity α. Forces are represented by lines, whose thickness is proportional to the force magnitude. Again, it can be seen that the structure of the force network is heavily dependent on contact parameters. It can be seen that the network's anisotropy increases with μ_s. Moreover, it can be observed that both μ_s and α enhance the formation of force chains, and these force chains tend to carry large forces along the principal stress direction. So, anisotropy is evident, not only regarding contact orientation but also force magnitude. As will be shown below, the anisotropic nature of this network can be directly linked to the system's shear strength.

Let us start by briefly recalling the stress-force-fabric relationship allowing linking of the anisotropic nature of the contact and force networks to the macroscopic shear strength. Further explanations can be found in the following references [22,24,49]. Let us consider the normal vector $\boldsymbol{n}$ between two particles that touch each other. In 2D, $\boldsymbol{n}$ is parametrized

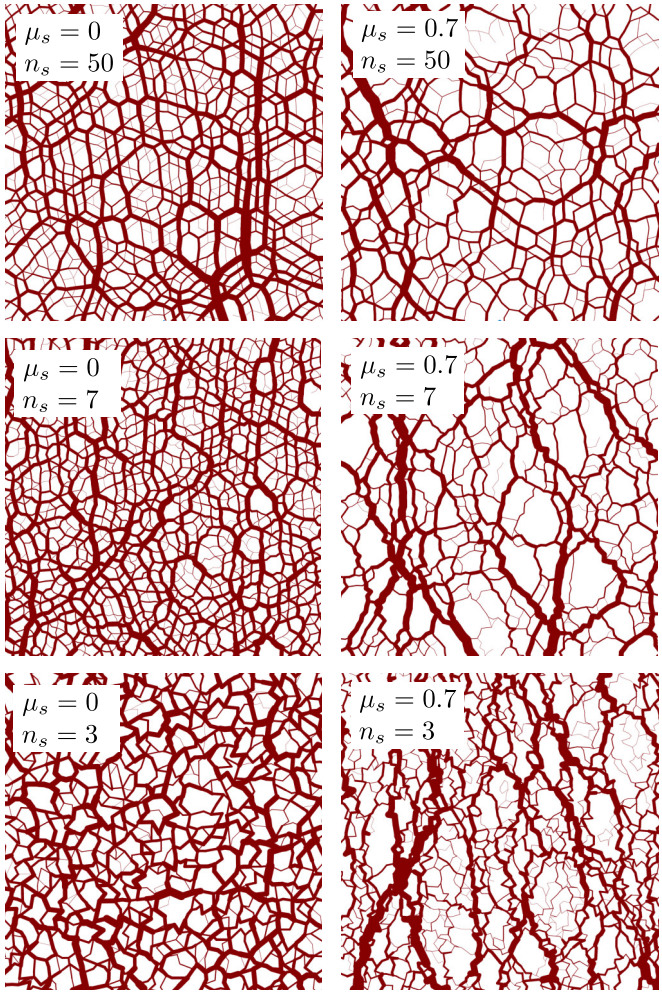

FIG. 8. Particle-scale views of the normal force network of six packings, for different values of local friction μ_s and particle angularity α. Forces are represented as lines, whose thickness is proportional to the force magnitude.

by a single angle. The probability density $P(\theta)$ of contact orientations θ encapsulates useful statistical information about the anisotropy of the contact network. Similarly, the contact forces $\boldsymbol{f}$ can be represented by their normal and tangential components as follows, $\boldsymbol{f} = f_n\boldsymbol{n} + f_t\boldsymbol{t}$. Thus, along with $P(\theta)$, averages $\langle f_n\rangle(\theta)$ and $\langle f_t\rangle(\theta)$ of normal and tangential forces provide the suitable statistical tools to describe the anisotropic state of a granular material.

As an example, Fig. 9 shows functions $P(\theta)$, $\langle f_n\rangle(\theta)$, and $\langle f_t\rangle(\theta)$ for packings composed of hexagons, for two values of local friction μ_s: 0.2 and 0.5. It can be seen that in the steady state the above functions tend to take a simple shape that is well approximated by a first order Fourier expansion:

$$\begin{cases} P(\theta) = \frac{1}{2\pi}\{1 + a_c \cos 2(\theta - \theta_c)\}, \\ \langle f_n\rangle(\theta) = \langle f_n\rangle\{1 + a_{fn} \cos 2(\theta - \theta_{fn})\}, \\ \langle f_t\rangle(\theta) = \langle f_n\rangle a_{ft} \sin 2(\theta - \theta_{ft}), \end{cases} \tag{4}$$

where a_c is the contact orientation anisotropy, a_{fn} the normal force anisotropy, and a_{ft} the tangential force anisotropy.

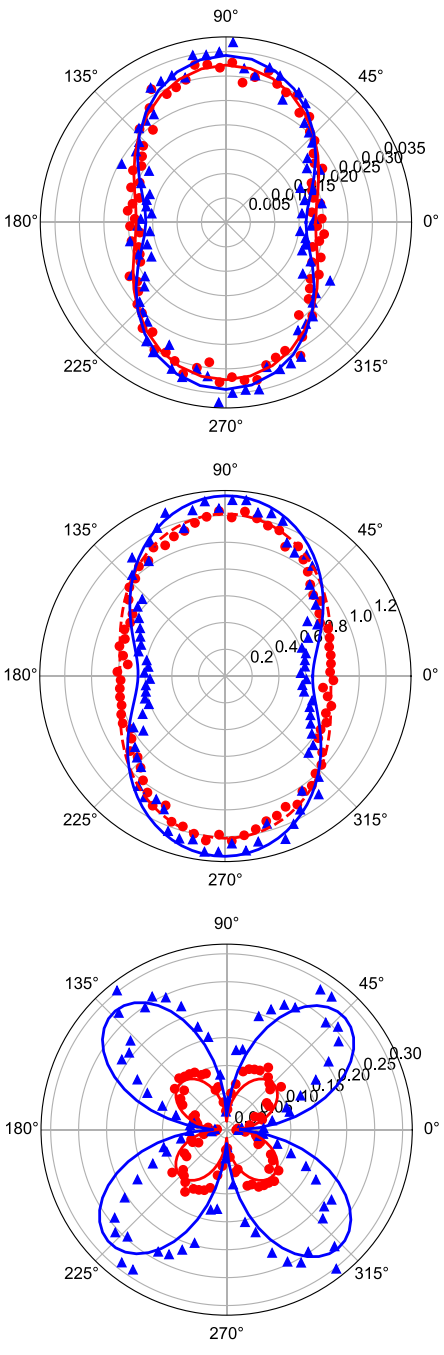

FIG. 9. Polar representation of: (a) probability density of contact orientations $P(\theta)$, (b) mean normal force $\langle f_n \rangle(\theta)$, and (c) mean tangential force $\langle f_t \rangle(\theta)$, as functions of contact orientation θ. Blue and red lines show the approximations given by Eq. (4) for packings composed of hexagons, for two values of the local friction μ_s, 0.5 and 0.2, respectively.

The angles θ_c, θ_{fn}, and θ_{ft} are the corresponding privileged directions, which coincide with the major stress direction $\theta_\sigma = \pi/2$. It should be noted that in practice anisotropic parameters are calculated through the force and fabric tensors, as presented in Ref. [22]. The analytical form of $\langle f_t \rangle(\theta)$ results from the orthonormal nature of the Fourier basis and the fact

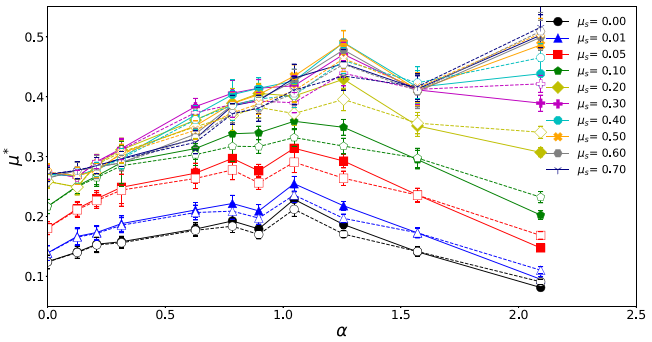

FIG. 10. Macroscopic friction coefficient μ^* as a function of the particle angularity α, for all values of the local friction μ_s (full symbols), together with the prediction given by Eq. (5) (dashed lines). Error bars represent the standard deviation in the steady state.

that the mean $\langle f_t \rangle$ value vanishes as a consequence of force balance.

Considering the expression of the stress tensor and after some mathematical manipulations and hypotheses (e.g., neglecting cross products between anisotropy parameters and assuming a low span in particle size distribution), the following simple relationship is obtained [22,49]:

$$\mu^* \simeq \tfrac{1}{2}(a_c + a_{fn} + a_{ft}). \tag{5}$$

Equation (5) highlights the key role of anisotropy parameters, as a means to explain the micromechanical origins of shear strength. Figure 10 shows the macroscopic friction coefficient μ^* as a function of α, for all values of μ_s, together with the prediction given by Eq. (5). It can be seen that the approximation is almost perfect, even for the most angular shapes. Therefore, it is interesting to analyze the effects of both μ_s and α on the evolution of a_c, a_{fn}, and a_{ft}, to shed light on the physical origins of the nonlinear variation of μ^*.

Figures 11 and 12 show the contact and force anisotropies, a_c, a_n, and a_t, as functions of both μ_s and α (insets). For all shapes, all anisotropies first increase with μ_s and then saturate at a shape-dependent value. This response underlies the observed increase and saturation of the macroscopic friction coefficient μ^* with μ_s. These trends are to be expected, for the following reasons. First, a_c increases with μ_s, indicating that

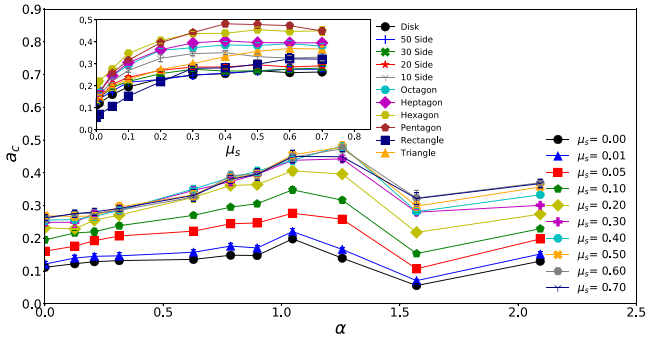

FIG. 11. Contact orientation anisotropy a_c as a function of both the particle angularity α and the local friction μ_s (inset). Error bars represent the standard deviation in the steady state.

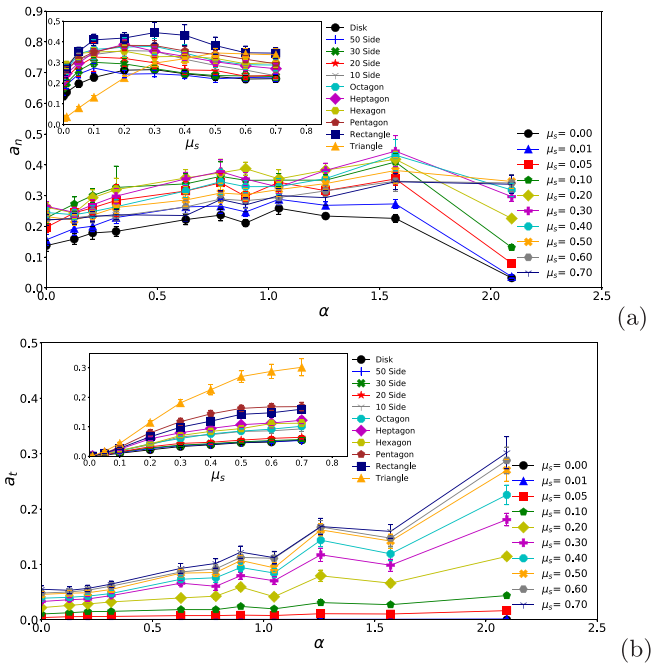

FIG. 12. Normal force anisotropy a_{fn} (a) and tangential force anisotropy a_{ft} (b) as functions of both the particle angularity α and the local friction μ_s (insets). Error bars represent the standard deviation in the steady state.

contact are being lost in the extension direction (see Figs. 8, 6, and 9). Then, a_{fn} increases with μ_s as force chains become more and more anisotropic (see Figs. 8 and 9). Finally, a_{ft} also increases with μ_s (see Fig. 9), showing that the stability of force chains is built upon an increasing mobilization of friction forces (in fact, $a_{ft} \propto \langle|f_t|\rangle/\langle f_n\rangle$ [24,50]). In contrast, the evolution of anisotropy with α is more complex as it also depends on μ_s. For all values of μ_s, a_c and a_{fn} initially increase with α and then decline as angularity increases. a_{ft} is an increasing function of α for all frictions, increasing faster as friction becomes greater.

By analyzing the anisotropy parameters, it can be shown that the observed increase of μ^* at low angularities and for all frictions is due to an increase of all anisotropies. For larger angularities, different mechanisms come into play depending on the local friction values. At low frictions, the decrease of μ^* with α is mainly due to the rapid falloff of the contact and normal force anisotropies, which is related to an excess of contacts. In particular, the force network of assemblies of triangles is nearly isotropic (i.e., $a_n \sim 0$). This explains why the macroscopic friction of such a system is smaller than that of a packing of disks. The nearly isotropic nature of the force network in packing of frictionless triangles, while the system is sheared, is also clearly evidenced in Fig. 8. Finally, for greater frictions the decrease of contact anisotropy is smaller than the increase of tangential force anisotropy, which leads to the continuous increase of μ^* with α.

V. CONCLUDING REMARKS

To sum up, using 2D contact dynamics simulations, we conducted a systematic analysis of the combined effects of local friction and particle shape on the quasistatic rheology of sheared granular materials. The local friction coefficient was varied from 0 (frictionless systems) to 0.7, and the shape of the particles was varied from disks to triangles. We only considered packings composed of polygonal particles, since their shape can be easily controlled through the number of sides.

A central finding of this work is that the effect of local friction on the shear strength follows the same trend for all shapes, i.e., it first increases with local friction and then saturates at a shape-dependent value. In contrast, the effect of the particle angularity on the shear strength depends on the level of sliding friction. For low frictions, the strength first increases with angularity but surprisingly it declines for the most angular shapes. This means that a weakly frictional packing composed of extremely angular particles can have a shear strength that is smaller than that of a packing of disks. For high frictions, the strength systematically increases with angularity. Interestingly, the evolution of the packing fraction with friction and shape is found to be almost inverse relative to that of the shear strength, implying that the densest systems are not necessarily those with the highest shear strength.

We showed that local friction and particle shape strongly affect the systems' microstructure in terms of the connectivity and the texture of the contact and force networks. Again, the effects of local friction follow the same trend, regardless of the particle shape, whereas the effects of angularity change depending on the value of local friction. In general terms, increasing the local friction causes networks to be less connected and more anisotropic. In contrast, increasing the particle angularity may change the topology of the networks in different directions, directly affecting the macroscopic shear strength. Specifically, we found that the nonlinear evolution of shear strength observed for the largest values of angularity is mainly due to compensation mechanisms between geometrical and mechanical anisotropies.

In the specific case of frictionless grains, it could be seen that a non zero shear strength was exhibited, but no dilatancy. These results are important, since they extend to the family of polygonal grains previous results obtained for disks [43], pentagons [31], and spheres [30]. In a broader context, it is worth mentioning that it was recently conjectured that the absence of dilatancy in frictionless systems can be at the origin of discontinuous shear thickening in some dense suspensions [51–54]. Our analyses support such hypothesis for suspensions composed of nonspherical particles.

Our perspective is to extend our analyses to other types of shapes, in particular elongated ones. Such analyses and data sets should constitute a first step toward a model able to predict macroscopic properties from the joint effect of local variables such as friction and grain shape.

ACKNOWLEDGMENTS

This work was supported by Royal Golden Jubilee Ph.D. Program (Grant No. PHD/0062/2558) under Thailand Research Fund (TRF) and French Embassy in Thailand. It was also supported by the project Ecos Nord C19P01/63672, for scientific cooperation between France and Colombia.

[1] J.-K. Mitchell and K. Soga, *Fundamentals of Soil Behavior* (Wiley, New York, 2005).
[2] A. Skinner, Geotechnique **19**, 150 (1969).
[3] N. Abriak, Math. Comput. Model. **28**, 121 (1998).
[4] L. Oger, S. Savage, D. Corriveau, and M. Sayed, Mech. Mater. **27**, 189 (1998).
[5] S. J. Antony and M. A. Sultan, Phys. Rev. E **75**, 031307 (2007).
[6] N. Estrada, A. Taboada, and F. Radjaï, Phys. Rev. E **78**, 021301 (2008).
[7] X. Huang, K. J. Hanley, C. O'Sullivan, and C. Y. Kwok, Int. J. Numer. Anal. Methods Geomech. **38**, 1276 (2014).
[8] J. Gong, J. Zou, L. Zhao, L. Li, and Z. Nie, Comput. Geotechnics **113**, 103105 (2019).
[9] K. M. Salerno, D. S. Bolintineanu, G. S. Grest, J. B. Lechman, S. J. Plimpton, I. Srivastava, and L. E. Silbert, Phys. Rev. E **98**, 050901(R) (2018).
[10] Z. Lu, A. Yao, A. Su, X. Ren, Q. Liu, and S. Dong, Eng. Geol. **253**, 36 (2019).
[11] Y. Zhu, Z. Nie, and J. Gong, Particuology **52**, 67 (2020).
[12] J. Bardet, Mech. Mater. **18**, 159 (1994).
[13] A. Tordesillas and D. Walsh, Powder Technol. **124**, 106 (2002).
[14] H. Zhu and A. Yu, Physica A: Stat. Mech. Appl. **325**, 347 (2003).
[15] M. Jiang, H.-S. Yu, and D. Harris, Comput. Geotechnics **32**, 340 (2005).
[16] Z. Chen, M. Omidvar, K. Li, and M. Iskander, Int. J. Phys. Model. Geotechnics **17**, 23 (2017).
[17] A. Mohamed and M. Gutierrez, Granular Matter **12**, 527 (2010).
[18] Y. Wang, F. Alonso-Marroquin, S. Xue, and J. Xie, Particuology **18**, 35 (2015).
[19] Y. Liu, H. Liu, and H. Mao, Granular Matter **20**, 12 (2018).
[20] W. Wu, G. Ma, W. Zhou, D. Wang, and X. Chang, Granular Matter **21**, 88 (2019).
[21] N. Estrada, E. Azéma, F. Radjai, and A. Taboada, Phys. Rev. E **84**, 011306 (2011).
[22] E. Azéma and F. Radjaï, Phys. Rev. E **81**, 051304 (2010).
[23] E. Azéma, N. Estrada, and F. Radjaï, Phys. Rev. E **86**, 041301 (2012).
[24] E. Azéma, F. Radjai, and F. Dubois, Phys. Rev. E **87**, 062203 (2013).
[25] M. Boton, E. Azéma, N. Estrada, F. Radjaï, and A. Lizcano, Phys. Rev. E **87**, 032206 (2013).
[26] E. Azéma, F. Radjaï, B. Saint-Cyr, J.-Y. Delenne, and P. Sornay, Phys. Rev. E **87**, 052205 (2013).
[27] S. Zhao and X. Zhou, Granular Matter **19**, 1 (2017).
[28] J. Gong and J. Liu, Particuology **32**, 49 (2017).
[29] Z. Nie, C. Fang, J. Gong, and Z. Liang, Comput. Geotechnics **121**, 103457 (2020).
[30] P.-E. Peyneau and J.-N. Roux, Phys. Rev. E **78**, 011307 (2008).
[31] E. Azéma, F. Radjaï, and J.-N. Roux, Phys. Rev. E **91**, 010202(R) (2015).
[32] E. Azéma, F. Radjaï, and J.-N. Roux, Eur. Phys. J. E **41**, 2 (2018).
[33] J. J. Moreau, Eur. J. Mech., A/Solids **13**, 93 (1994).
[34] F. Radjai and F. Dubois, *Discrete-Element Modeling of Granular Materials* (Wiley, New York, 2011).
[35] F. Dubois, V. Acary, and M. Jean, Comptes Rendus Mécanique **346**, 247 (2018).
[36] M. Renouf, F. Dubois, and P. Alart, J. Comput. Appl. Math. **168**, 375 (2004).
[37] F. da Cruz, S. Emam, M. Prochnow, J.-N. Roux, and F. Chevoir, Phys. Rev. E **72**, 021309 (2005).
[38] D.-H. Nguyen, E. Azéma, P. Sornay, and F. Radjai, Phys. Rev. E **91**, 032203 (2015).
[39] A. Taboada, K.-J. Chang, F. Radjaï, and F. Bouchette, J. Geophys. Res. **110**, B09202 (2005).
[40] GDR MiDi, Eur. Phys. J. E **14**, 341 (2004).
[41] B. Andreotti, Y. Forterre, and O. Pouliquen, *Granular Media: Between Fluid and Solid* (Cambridge University Press, Cambridge, 2013).
[42] J.-J. Moreau, in *Micromechanics of Granular Materials*, edited by B. Cambou, M. Jean, and F. Radjai (ISTE, London, UK, 2009), pp. 51–100.
[43] N. Estrada, Phys. Rev. E **94**, 062903 (2016).
[44] A. Taboada, N. Estrada, and F. Radjaï, Phys. Rev. Lett. **97**, 098302 (2006).
[45] I. Agnolin and J.-N. Roux, Phys. Rev. E **76**, 061302 (2007).
[46] M. van Hecke, J. Phys.: Condens. Matter **22**, 033101 (2009).
[47] D.-H. Nguyen, E. Azéma, F. Radjai, and P. Sornay, Phys. Rev. E **90**, 012202 (2014).
[48] T. A. Marschall and S. Teitel, Phys. Rev. E **100**, 032906 (2019).
[49] L. Rothenburg and R. J. Bathurst, Geotechnique **39**, 601 (1989).
[50] Z. Nie, Y. Zhu, X. Wang, and J. Gong, Granular Matter **21**, 22 (2019).
[51] R. Seto, R. Mari, J. F. Morris, and M. M. Denn, Phys. Rev. Lett. **111**, 218301 (2013).
[52] M. Wyart and M. E. Cates, Phys. Rev. Lett. **112**, 098302 (2014).
[53] D. Vågberg, P. Olsson, and S. Teitel, Phys. Rev. E **95**, 052903 (2017).
[54] C. Clavaud, A. Bérut, B. Metzger, and Y. Forterre, Proc. Natl. Acad. Sci. USA **114**, 5147 (2017).